STUDYING EXTREME ULTRAVIOLET WAVE TRANSIENTS WITH A DIGITAL LABORATORY: DIRECT COMPARISON OF EXTREME ULTRAVIOLET WAVE OBSERVATIONS TO GLOBAL MAGNETOHYDRODYNAMIC SIMULATIONS

Cooper Downs[1], Ilia I. Roussev[1], Bart van der Holst[2], Noé Lugaz[1], Igor V. Sokolov[2], and Tamas I. Gombosi[2]
[1] Institute for Astronomy, University of Hawaii, at Manoa, 2680 Woodlawn Dr., Honolulu, HI 96822, USA; cdowns@ifa.hawaii.edu
[2] Center for Space Environment Modeling, University of Michigan, 2455 Hayward St., Ann Arbor, MI 48109, USA

ABSTRACT

In this work, we describe our effort to explore the signatures of large-scale extreme ultraviolet (EUV) transients in the solar corona (EUV waves) using a three-dimensional thermodynamic magnetohydrodynamic model. We conduct multiple simulations of the 2008 March 25 EUV wave (∼18:40 UT), observed both on and off of the solar disk by the *STEREO-A* and *B* spacecraft. By independently varying fundamental parameters thought to govern the physical mechanisms behind EUV waves in each model, such as the ambient magneto-sonic speed, eruption free energy, and eruption handedness, we are able to assess their respective contributions to the transient signature. A key feature of this work is the ability to synthesize the multi-filter response of the *STEREO* Extreme UltraViolet Imagers directly from model data, which gives a means for direct interpretation of EUV observations with full knowledge of the three-dimensional magnetic and thermodynamic structures in the simulations. We discuss the implications of our results with respect to some commonly held interpretations of EUV waves (e.g., fast-mode magnetosonic wave, plasma compression, reconnection front, etc.) and present a unified scenario which includes both a wave-like component moving at the fast magnetosonic speed and a coherent driven compression front related to the eruptive event itself.

Key words: magnetohydrodynamics (MHD) – Sun: corona – Sun: coronal mass ejections (CMEs) – Sun: magnetic topology – waves

1. INTRODUCTION AND BACKGROUND

One of the most paradoxical themes in the study of our nearest star is that of its proximity: while we are treated to an unprecedented view of the solar atmosphere afforded by front row seats from Earth, it is this view that offers up a litany of complex and dynamic astrophysical structures, which are often ambiguous in their interpretation. This is particularly true for the case of the low solar corona ($r < 1.4\,R_\odot$) when imaged in the extreme ultraviolet (EUV) regime. The highly nonlinear temperature and density dependence of commonly observed coronal emission lines (e.g., Fe ix 171 Å, xii 195 Å, and xv 284 Å) combined with line-of-sight projection effects inherent when observing optically thin EUV coronal structures often makes interpretation of conspicuous phenomena difficult.

With these sentiments in mind, our focus in this work is the study and interpretation of large-scale coronal transients known as EUV waves. Originally named EIT waves (Moses et al. 1997), because they were first observed by the EUV Imaging Telescope (EIT; Delaboudinière et al. 1995) on board the *Solar and Heliospheric Observatory* (*SOHO*) spacecraft, they are characterized by a diffuse rim of enhanced EUV emission expanding outward from an eruption site located within a coronal active region (AR). EUV waves in the corona are typically observed during the onset of a solar flare and/or a coronal mass ejection (CME) and are occasionally temporally related to Moreton waves in the chromosphere (Khan & Aurass 2002), which are observed in H$_\alpha$ line images. Additionally, shocks formed by EUV waves (when propagation exceeds the local magnetosonic speeds) can provide an acceleration mechanism for solar energetic particles and associated radio bursts as they travel away from the eruption site (Klassen

et al. 2000). For clarity in the ensuing discussion, we choose to adopt the Cohen et al. (2009) convention of referring to these phenomena as "EUV waves," a general term, one which naturally includes observations from the modern generation of EUV imagers, rather than the conventional term "EIT waves," a specific reference to the EIT instrument.

EUV waves are interpreted by many as fast magnetosonic waves in the coronal plasma (e.g., Thompson et al. 1999; Wu et al. 2001; Warmuth et al. 2005; Long et al. 2008; Patsourakos et al. 2009b; Veronig et al. 2010), a logical explanation considering their typical propagation speed (200–400 km s^{-1}) is plausibly of the order of the fast magnetosonic speed, c_f, in quiescent closed field regions of the corona (referred to as the "quiet-Sun"). The wave nature of EUV waves is also often invoked to explain the reflection of these fronts off of regions with large gradients in magnetosonic speed, such as interface between quiet-Sun and open field regions (coronal holes) with large ambient values of c_f (Gopalswamy et al. 2009; Schmidt & Ofman 2010). Also, a recent study involving simultaneous observations of an EUV wave from multiple locations (Patsourakos & Vourlidas 2009a) offered the observed lack of co-spatiality of the erupting CME cavity and EUV wave transient as further confirmation of the fast-mode wave scenario.

However, this interpretation is not unique. One of the major difficulties in interpreting EUV waves is the fact that their signature is simultaneously coupled with the dynamic evolution of the structure of the corona (as must be the case for CMEs) and limited by image projection effects due to the three-dimensional structure of the event (Ma et al. 2009). As instability sets in during a CME, interaction of the erupting field with the overlying flux systems and the impingement of expanding plasma on the surrounding environment are necessary by-products. This

zeroth-order change of the environment complicates the interpretation of these transients as simply a linear first-order transient over the background field (Attrill et al. 2009). For example, the same set of observations of the 2007 May 19 EUV wave transient have produced evidence both for fast-mode wave reflection (Gopalswamy et al. 2009) and against (Attrill 2010). Evidence combining these elements have also been found in numerical experiments that resolve a fast-mode wave component and a component related to coronal restructuring due to the CME itself (Chen et al. 2002, 2005; Cohen et al. 2009). Additionally, a scenario proposing that reconnection between the favorably aligned quiet-Sun field and the legs of the expanding CME magnetic structure is the primary cause of the diffuse front has been argued both theoretically (Attrill et al. 2007) and observationally through a study of multi-wavelength EUV imaging data Dai et al. (2010)). Other nonlinear magnetohydrodynamic (MHD) modes e.g., the slow mode shock component of a Moreton wave (Wang et al. 2009) and the solitary wave solution described by Wills-Davey et al. (2007) have also been invoked to explain the diffuse front of EUV waves. For a comprehensive review of EUV wave observations and their interpretations, please refer to Wills-Davey & Attrill (2009) and Patsourakos et al. (2009b).

One property of the purely fast-mode wave interpretation of EUV waves that we wish to highlight is the requirement that the perturbation travels at c_f or above in the case of shocks, where $v_a < c_f < \sqrt{v_a^2 + c_s^2}$ and $v_a = |\vec{B}|/\sqrt{4\pi\rho}$ is the local Alfvén speed and $c_s = \sqrt{P/\gamma\rho}$ is the local sound speed. This sets a stringent requirement on a parameter that is both spatially inhomogeneous and not well constrained through inferences (Wills-Davey et al. 2007 give 215 km s^{-1} $<$ $c_f < 1500$ km s^{-1} as plausible values for c_f in the quiet-Sun). This requirement is also called into question by Yang & Chen (2010), who find a negative correlation of magnetic field strength with derived EUV wave speeds for two events, which is opposite to the expected result for a purely fast-mode MHD wave.

Ultimately one thing is clear: because the dynamics of wave propagation speed and shock formation depend highly upon the local sound and Alfvén speeds, the thermal-magnetic structure of the corona is critically important for any EUV wave theory. Combining these elements in a fully dynamic model to probe nonlinear or non-wave scenarios in unison is then critical in furthering our ability to construct and constrain a theoretical framework for these events. Moreover, it is equally important for the results of any EUV wave scenario to be directly interpreted in the context of actual observations. From this perspective, we present a series of simulations of a realistic EUV wave using a global three-dimensional thermodynamic MHD model of the corona. We examine the effect that three key variables (eruption strength, eruption handedness, and ambient quiet-Sun magnetosonic speed) have on the ensuing transient signature, which is synthesized for direct comparison to observations. While in a sense we are changing these parameters to "see what happens," in our minds, this is a critical use of computational models, i.e., as an ideal laboratory to study physical mechanisms in a controlled manner.

In Section 2, we describe the observations of the 2008 March 25 EUV wave transient, the prototypical event that we have chosen. In Section 3, we describe the three-dimensional MHD model and methods used in this work. Sections 4 and 5 describe the simulation runs and our interpretation of their results. We conclude in Section 6.

2. OBSERVATIONS

2.1. The 2008 March 25 EUV Wave Event

The focus of this work is the conspicuous EUV wave transient that occurred on 2008 March 25 around 18:40 UT, with the eruption/flare site centered on NOAA AR 10989. Observed directly by the Sun Earth Connection Coronal and Heliospheric Investigation (SECCHI) instruments (Howard et al. 2008) on board the *STEREO-A* and *STEREO-B* spacecraft pair (Kaiser et al. 2008) as well as the *SOHO* spacecraft, this event produced a GOES M1.7 class flare and was associated with a modest CME (Aschwanden 2009; Patsourakos et al. 2010). With *STEREO-A* and *STEREO-B* separated at this time by $\sim 47°$, the Extreme UltraViolet Imagers (EUVI; Wuelser et al. 2004) on board produced synced observations of the entire event in four EUV filters at a high cadence (~ 2.5 minutes cadence for the Fe IX 171 Å and He II 304 Å filterbands, and 5 minutes cadence for the Fe XII 195 Å and Fe XV 284 Å filterbands). This arrangement afforded a dynamically rich view of the event, seen in projection both off of the east limb (*STEREO-A*) and on the disk (*STEREO-B*). At this time the erupting AR was only slightly behind the east limb as seen by *STEREO-A*. This afforded optimal viewing conditions of the transient evolution-off of the limb of the solar disk and highlights the north/south propagation of the transient. For this reason, we choose focus on the EUVI-A data set in this work. Five minute running ratio snapshots, created by dividing the pixel-by-pixel flux of an EUVI image by a preceding image nearest to a given time interval, are shown for EUVI-A observations in the 171, 195, and 284 Å filters for the first 45 minutes of the event in Figure 1.

The running ratio method (the same as that used by Patsourakos et al. 2009b) is chosen because ratios highlight relative changes in photon flux that are independent of the absolute flux value, unlike the more commonly used difference technique that compares a flux difference (e.g., Dai et al. 2010; Gopalswamy et al. 2009; Wills-Davey et al. 2007). This makes ratio images effective for visualizing the EUV wave signal off of the solar disk, where EUV flux drops off drastically (note that the emission of the Fe lines contributing to the EUVI filters is proportional to electron density squared in the collisional regime of the low corona). This implies that running ratio images effectively divide out the density dependence of the transient as a function of height, whereas running difference images do not. In the context of this analysis, we choose running ratios as opposed to base ratios (where each image is divided by a pre-event image) in order to best focus on the large-scale evolution of the transient with respect to itself at large distances. While base methods applied to limb events are optimal for studying coronal dimming and determining CME mass (e.g., Aschwanden et al. 2009), they are not appropriate for studying the evolution of the extended EUV wave front away from the source region at times beyond ~ 20 minutes of the beginning of the event. This is due to the non-negligible rotation of extended structures off of the limb adding spurious contributions to the measurement that grow in amplitude with time for base methods, while this contribution is fixed for running methods. Additionally, to enhance the large-scale properties of the event and smooth out the effects of photon noise off of the limb, we perform Gaussian convolution of each EUVI image with a half width of $\sigma = 0.005 R_\odot$ (~ 3 pixels) before calculating the ratios. A prototypical EUV wave event is characterized first by an outward hemispherical enhancement front and strong dimming in the eruption region. As the outward front leaves the field of view of the instrument,
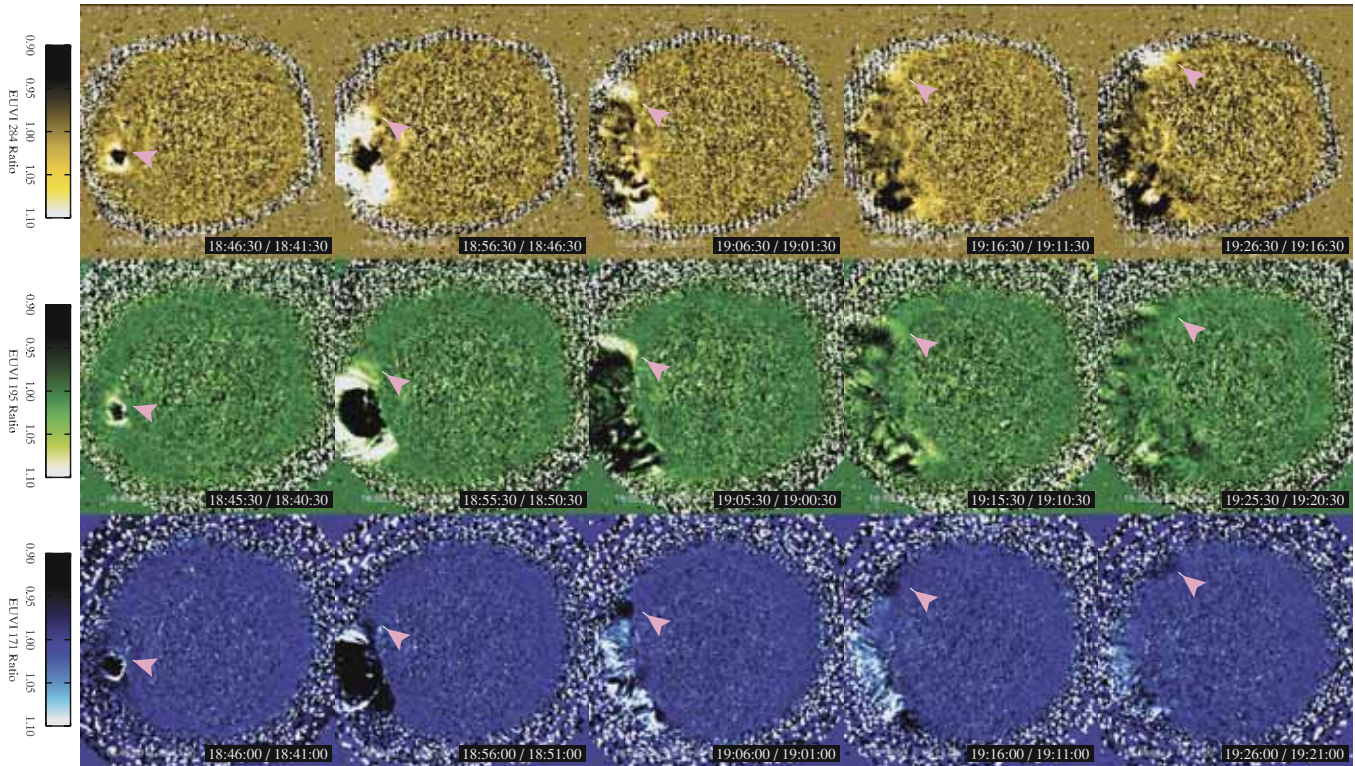
Figure 1. Running ratio images at 5 minute intervals for the first 45 minutes of the 2008 March 25 EUV wave event in the EUVI 171 Å (bottom) 195 Å (middle) and 284 Å (top) wavebands. The approximate location of the northward propagating front at each time is shown with an arrow. The speckled pattern beyond $r \sim 1.3\ R_\odot$ is due to photon noise and data compression. As is the characteristic of EUV wave transients, these observations show a diffuse front expanding over large transverse distances within a short period of time. There is also a clear anti-correlation of the sign of the perturbation between the 171 Å filter and 195 Å and 284 Å filters within the front. Note that the second and last frames for the 284 Å filter are shown as a 10 minute running ratio due data gaps.

the transient retains a conspicuous transverse component in the form of a wave-like diffuse front that reaches the northern coronal hole at around $t \sim 19{:}15$–$19{:}30$ UT.

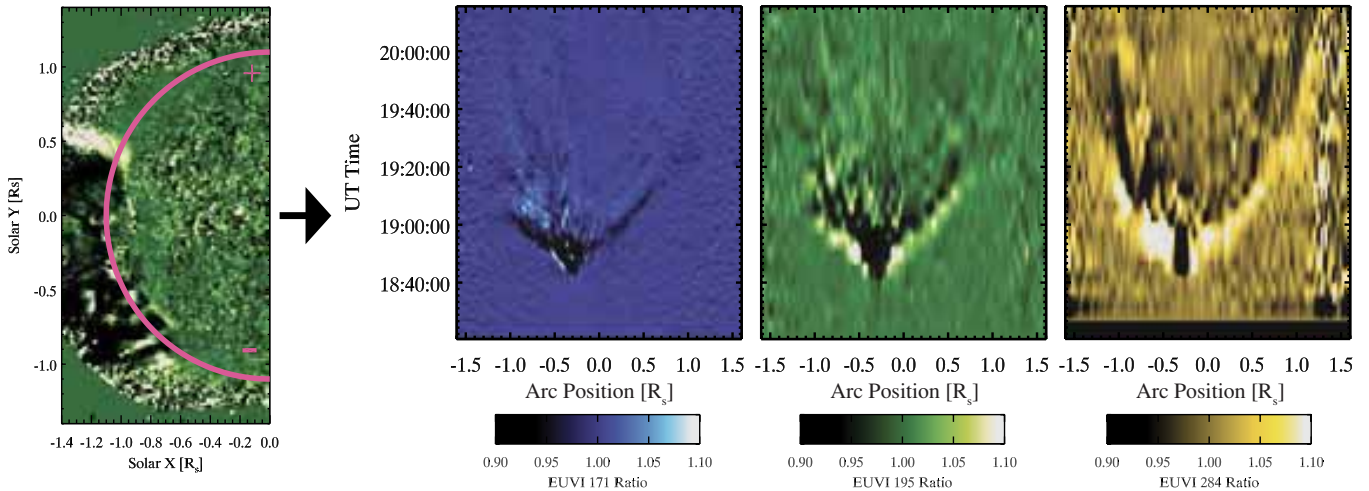### 2.2. Time–Distance Limb Diagrams

One of our main tools for analyzing the dynamics of the March 25 EUV wave is the time–distance diagram. Analogous to the time–elongation plot commonly used to track CMEs with coronagraph observations (e.g., Sheeley et al. 2008; Lugaz et al. 2009), we construct these diagnostics by first extracting the EUV signal along a Sun-centered circular arc of radius $r = 1.1\ R_\odot$ off of the East limb for every image in the dataset. The ratio of the EUV flux along this arc to the flux for the preceding image for a given filter is then calculated. These ratios now form a two-dimensional grid with distance, s, along the arc as the x-axis and time as the y-axis, from which the speed of the projected bright EUV front at a given radius can be directly calculated from the slope. A schematic of this process is shown in Figure 2 (left), and the time–distance limb diagrams for the EUVI-A 171, 195, and 284 Å filters are shown in Figure 2 (right).

Immediately apparent upon examination of the EUVI-A time–distance diagrams is both the apparent speed (common in all three) and contrasting amplitudes for a fixed location between each filter (i.e., temperature window). Toward the north pole (positive x-axis), the 171 and 195 Å filters exhibit anti-correlated behavior, suggestive of a heating/relaxation period where the average temperature within the bright front is enhanced and subsequently cools as the transient passes. A simple estimate of the slope of the maximum enhancement in the 284 Å filter between the points $s_1 = 0.18\ R_\odot$ and $s_1 = 0.56\ R_\odot$ gives a front speed of ~ 350 km s^{-1}, although this measurement is

limited mainly by ratio cadence and inherent uncertainty in the flux values due to the ambient evolution of the corona. We show a zoomed-in view of the time–distance diagrams for the northward front with an overplotted speed range to demonstrate these features in Figure 3.

3. NUMERICAL MODEL

The numerical tool used in this work is the lower corona (LC) component of the Space Weather Modeling Framework (SWMF), a fully parallelized, customizable three-dimensional MHD modeling framework (a general overview can be found in Tóth et al. 2005). Details of the development and application of the LC component, which includes considerations relevant to resolving the thermodynamics of the low corona and transition region (e.g., radiative loss, field-aligned electron heat conduction, and empirical coronal heating in the energy equation), can be found in Downs et al. (2010). A critical feature of this tool and its previous iterations (e.g., Roussev et al. 2003; Cohen et al. 2007) is the ability to include synoptic magnetic observations of any Carrington rotation (CR; standard solar rotation number) as a boundary condition and a basis to extrapolate the three-dimensional magnetic field permeating the corona. This provides a means to study the conditions that are observed in the corona directly with an MHD model. For our simulations, the initial magnetic field configuration and boundary conditions are extrapolated via the potential field source surface method (PFSSM; Altschuler et al. 1977), using high-order radial magnetic coefficients derived from observations by the Michelson Doppler Imager (MDI) instrument aboard the *SOHO* observatory for CR 2068 centered on 2008 March 25.

Figure 2. Time–distance diagrams of the EUV transient observed by EUVI-A off of the limb for the EUVI-A 171 Å, 195 Å, and 284 Å filters. The x-axis, shown schematically as the magenta arc in the left inset, represents the position along an arc of constant radii, $r = 1.10\,R_\odot$, which spans the east limb with the equator as the zero point. The coloring of the time–distance diagrams (right) represents the flux ratio of the preceding image for points on this arc. Note that the cadence for the 171 Å was 2.5 minutes while the cadence for then 195 Å and 284 Å filters was 5 minutes (except for 10 minute gaps for times $t = 18{:}56{:}30$ and $19{:}26{:}30$ for the 284 Å filter). The aspect ratio is achieved through linear interpolation of the time-coordinate.
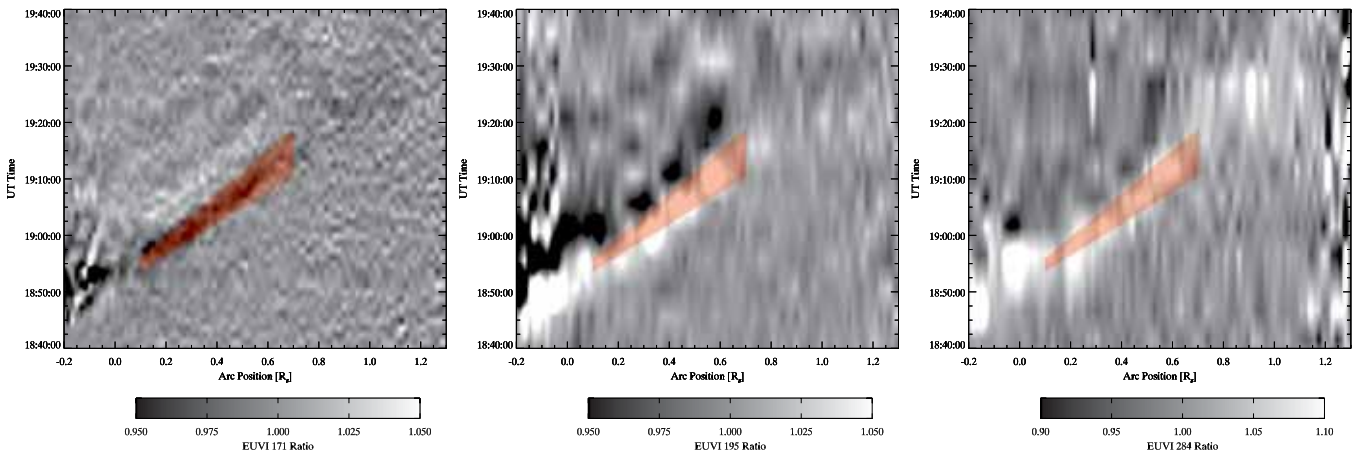

Figure 3. Time–distance diagrams of the EUV transient zoomed in on the northward front for the EUVI-A 171 Å, 195 Å, and 284 Å filters. The red transparent polygon represents the range of 350 ± 50 km s^{-1} overplotted on the front between $s = 0.1$ and $0.7\,R_\odot$, and is displayed at the same location in each frame. The slope of the polygon is defined by the bounding speed range while the width in time is defined by the time interval needed to travel at these speeds to $s = 0.1\,R_\odot$ from $s = -0.15\,R_\odot$, the approximate origin of the event from this point. Here we see the slope of the perturbation falls within this speed interval, and that the anti-correlated nature of the 171 Å perturbation to that in 195 and 284 Å in space and time along the front is clearly visible.

A particular advantage of the LC component is the ability to achieve realistic equilibrium temperatures and densities in the low corona without a strong dependence on the choice of boundary conditions. Here, the solar boundary is set in the chromosphere with characteristic values of electron density, n_e, and temperature, T_e ($n_{e,0} = 1 \times 10^{12}$ cm^{-3}, $T_{e,0} = 4 \times 10^4$ K), and a widened transition region is resolved by modifying the ratio of heat conduction to radiative cooling at temperatures below 300,000 K (see Lionello et al. 2001, 2009 for details). In this case, thermodynamic balance in the corona is achieved self-consistently due to the interplay between magnetic topology and thermodynamic energy balance in the transition region. This then lends itself naturally to directly calculating the expected EUV emission of the model corona (a strong function of local n_e and T_e) and using this to validate the results for a specific time relative to spacecraft observations in the EUV regime (Downs et al. 2010). The important details and modifications to the LC model for the study of EUV wave transients are described below.

3.1. Line-of-sight Image Synthesis

Perhaps the most important diagnostic to characterize our model results is the synthesis of EUV images for one-to-one comparison to spacecraft observations. The process for creating these images from three-dimensional simulation data for the *SOHO* EIT and *Yohkoh* Soft X-ray Telescope instruments is well described by Mok et al. (2005) and Lionello et al. (2009), and the particular application of this method to the LC model is described in Downs et al. (2010). To build upon this foundation, we implement the ability to synthesize observations for the modern EUVI instruments on board the *STEREO-A* and *B* spacecraft as well as the X-Ray Telescope (XRT) on board the *Hinode* spacecraft. This process is summarized as follows: a spectrum including continuum processes and optically thin emission lines important in the soft-X-ray to EUV regime (1–450 Å) is calculated for each point on a two-dimensional grid of n_e and T_e using the CHIANTI emission line analysis code (Landi et al. 2006; values ranging from 10^5 cm$^{-3} < n_e < 10^{12}$ cm^{-3} and
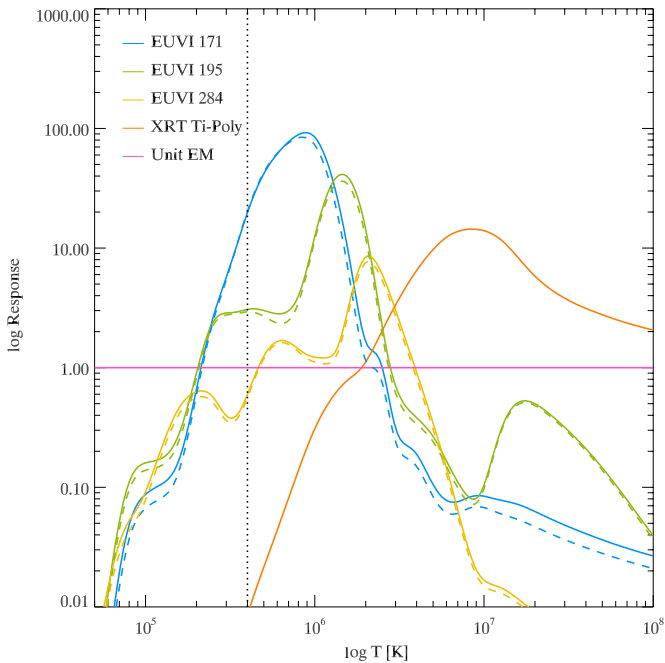
Figure 4. Temperature dependence of the filter response functions $R_i(n_e, T_e)$ for a fixed value of electron density, $n_e = 1 \times 10^8$ cm^{-3}. These functions used to generate the synthetic images for each run. The slightly differing response functions for the EUVI-A (solid) and EUVI-B (dashed) are also shown. The units of $R_i(n_e, T_e)$ are 10^{-26} photons s^{-1} cm^{-5}, 10^{-26} DN s^{-1} cm^{-5}, and 10^{-26} cm^{-5} for three EUVI filters, the XRT Ti-Poly filter, and the unit EM diagnostic, respectively. To neglect the unrealistic EM contribution of the widened transition region, we set the $R_i(n_e, T_e) = 0$ to the left of the dotted line at $T_e = 400,000$ K.

$10^{4.5}$ K $< T_e < 10^8$ K). For this step we use the composite abundance file `sun_coronal_ext.abund` and the composite ionization equilibrium file `arnaud_raymond_ext.ioneq` (distributed with the CHIANTI database) to calculate these spectra. Then, using the calibration data for the EUVI and XRT instruments provided by the SECCHI and *Hinode* teams to the SolarSoft framework (Freeland & Handy 1998), we calculate the expected response per pixel, $R_i(n_e, T_e)$, for a unit column emission measure (EM, units of cm^{-5}) for each specific instrument and filter (we model the EUVI 171 Å, 195 Å, 284 Å, and XRT Ti-Poly filters in this work). The total flux measured by a pixel then takes the form of

$$F_{\text{los}} = \int n_e^2 R_i(n_e, T_e) dl \quad (\text{counts s}^{-1}), \tag{1}$$

where the integral is carried over the unique line of sight of the pixel through the corona, and the unit of measurement, "counts," depends on the particular choice of units for $R_i(n_e, T_e)$. As an additional aid in decoupling the temperature dependence of these diagnostics, we also produce images of the integrated column EM for each pixel, which amounts to using the same synthesis method with $R_{\text{EM}}(n_e, T_e) = 1 \times 10^{-26}$ cm^{-5}. To avoid integrating through artificially high EM regions which are produced in the widened transition region, we cut off each response function for temperatures below $T_e = 400,000$ K. The temperature dependence of $R_i(n_e, T_e)$ for each filter at a fixed value of n_e is shown in Figure 4.

3.2. Heating Model

As a proxy for the as yet unknown mechanisms of coronal heating, we include a simple but effective multi-component

empirical coronal heating source term to the MHD energy equation in order to achieve acceptable agreement of the relaxed MHD configuration to EUV observations. This term takes the form $Q_{\text{total}} = Q_{\text{qs}} + Q_{\text{ch}} + Q_{\text{ar}}$. The first two terms are identical to those previously explored by Downs et al. (2010) and use a simple exponential decay model of the form $Q_h = H_0 \exp[-(r - R_\odot)/\lambda]$.

Before further discussing the individual heating terms, it is worth noting here that due to (1) the significant amount of computation required to advance a time-dependent three-dimensional thermodynamic MHD model and (2) the lack of a universally agreed upon first-principles coronal heating mechanism, we must necessarily use an empirical parameterization to represent coronal heating within the model. The previous work of Lionello et al. (2009) and Downs et al. (2010) explore heating functions in this context, demonstrating a favorable agreement with EUV observations through quantitative comparisons, and we base the heating functions and their parameter values on their results. Although in an ideal situation we would not hand-pick parameter values, a further refinement of these parameters through a rigorous deterministic approach, through e.g., a statistical Monte Carlo technique, would require a currently infeasible amount of computation time and would not be guaranteed to provide additional physical insight due to the inherently empirical and parameterized nature of the heating terms. With this sentiment in mind, a description of our chosen empirical heating terms and their physical purpose is given below.

Q_{qs} is intended to represent the average heating of closed field (quiet-Sun) systems in the corona, with heating concentrated near the base of the corona (small scale-height). We choose parameters $H_{0,\text{qs}} = 7.28 \times 10^{-5}$ erg cm^{-3} s^{-1} and $\lambda_{\text{qs}} = 25$ Mm, and apply this term to closed field regions only, which is determined from a ray-tracing of the initial PFSSM extrapolation of $\vec{B}$ (described below).

The Q_{ch} term is an attempt to grossly approximate the average effect of wave-heating mechanisms of the solar wind. Using parameter values of $H_{0,\text{ch}} = 5.00 \times 10^{-7}$ erg cm^{-3} s^{-1} and $\lambda_{\text{ch}} = 0.7$ $R_\odot$, this large scale-height heating term allows both for relatively low densities and temperatures within coronal holes near the Sun ($n_e \sim 5 \times 10^7$ cm^{-3}, $T_e \sim 900,000$ K, for $r = 1.04$ $R_\odot$), and reasonable temperatures (1 MK $< T_e <$ 2 MK) at distances beyond $r = 2.0$ $R_\odot$. This term is applied uniformly.

The last heating component, Q_{ar}, is designed to represent the presence of strong heating in ARs, particularly near loop footpoints and the polarity inversion region. Differing from the purely $|B|$-weighted form presented in Downs et al. (2010), this term is motivated by the linear relationship of loop heating to the ratio of basal field strength to loop length derived by Pevtsov et al. (2003; also explored by Schrijver et al. 2004). To implement this, we use an initial ray-tracing of the three-dimensional magnetic field to correlate a cell in three-dimensional space to its specific mapping on $\vec{B}$ to the Solar boundary at $r = 1.00$. Once determined, the boundary field magnitude is interpolated to this position and used to determine the strength of the heating term according to

$$Q_{\text{ar}} = \sum_{i=1}^{2} H_{\text{ar}} \exp(-L_i(\vec{x})/\lambda_{\text{ar}}),$$
$$H_{\text{ar}} = H_{0,\text{ar}} \min\left[\frac{B_{s,i}}{L_h}, \left(\frac{B_s}{L_h}\right)_{\text{max}}\right], \tag{2}$$
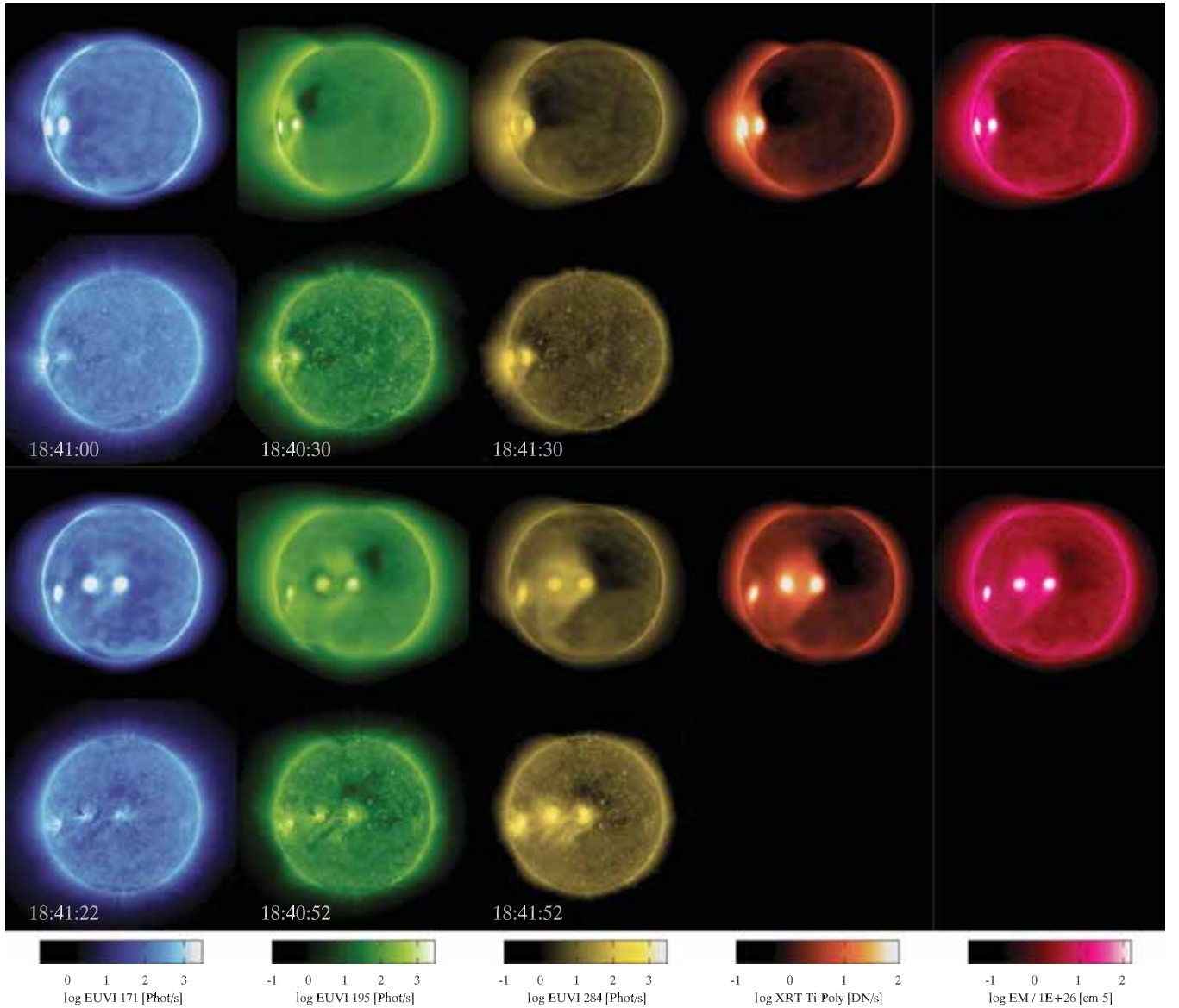
Figure 5. Comparison of synthetic LOS images for simulation Run A to EUVI-A (upper half) and B (lower half) observations. Shown in columns from left to right are the EUVI 171 Å, 195 Å, 284 Å filters, XRT Ti-Poly filter, and integrated EM. We use the synthetic XRT observations from these vantage points as a high temperature diagnostic (note that $R_{\mathrm{Ti-Poly}}$ is within 20% of its maximum for $T_e \sim > 2.8 \times 10^6$ K).

where the index i sums over each direction of the loop, $L_i(\vec{x})$ is the length of the loop traced from location $\vec{x}$ in the ith direction (parallel and anti-parallel to $\vec{B}$, respectively), L_h is the total loop half-length ($L_h = (L_1(\vec{x}) + L_2(\vec{x}))/2$), $B_{s,i}$ is the magnitude of the magnetic field strength where the trace intersects the boundary, $H_{0,\mathrm{ar}} = 1 \times 10^{-2}$ erg cm^{-3} s^{-1} sets the minimum AR heating rate, $\lambda_{\mathrm{ar}} = 20$ Mm defines the heating scale-height, and $(B_s/L_h)_{\mathrm{max}} = 20$ Gauss Mm^{-1} sets the maximal AR heating threshold. We find that this provides hot, high density plasma in equilibrium within the AR, and thus yields adequate results both when comparing AR emission on and off of the solar disk for the high temperature filters (284 Å and Ti-Poly). As a validation of the ability of this composite heating function to capture the thermodynamic state of the corona for 2008 March 25, a comparison of the synthetic images produced from our baseline run, Run A, to EUVI observations is shown in Figure 5 (details of this run are described in Section 4).

3.3. Eruption Model

In order to generate a strong EUV transient in our simulations, we use an eruption model that is tailored to the asymmetric conditions that occur regularly in the solar corona. Additionally, because our specific goal is to synthesize EUV images from time-dependent results and compare these to observations, it is critical that this model does not impose unrealistic temperature and density profiles at the source region.

We choose to use a form of the charge shearing eruption method introduced in Roussev et al. (2007) and further studied for an idealized configuration by Jacobs et al. (2009). In the bipolar version, additional magnetic flux is added to the positive and negative polarities of the approximate bipole compromising AR 10989 in the form of two magnetic charges, $+q$ and $-q$ (denoted $q_\pm$), placed at locations $\vec{x}_+$ and $\vec{x}_-$, 7Mm below the surface, which are perpendicular to the polarity inversion line of the bipole, and separated by an initial distance $L_0 = 15$ Mm.

Table 1
Summary of the Four Model Runs and the Choice of Parameters for Each Run

Run	$|q_{\pm}|$ (Gauss m^{-2})	Handedness	$\vec{B}$ scaling	$v_{\rm rise}$ (km s^{-1})	$v_{\rm peak}$ (km s^{-1})
A	2E+13	N/S	1	380 ± 30	240 ± 5
B	4E+13	N/S	1	440 ± 30	289 ± 8
C	2E+13	S/N	1	380 ± 60	123 ± 4
D	4E+13	N/S	2	780 ± 50	322 ± 15

Note. We also show the computed speeds of the two transverse fronts identified in the transient signal (described below).

In this case, the additional dipole field takes the functional form $\vec{B}_{q_{\pm}} = q_{\pm} \cdot (\vec{x} - \vec{x_{\pm}})/|\vec{x} - \vec{x_{\pm}}|^3$ (note that $\vec{B}_{\rm tot} = \vec{B}_{q_+} + \vec{B}_{q_-}$ automatically satisfies both $\nabla \cdot \vec{B}_{\rm tot} = 0$ and $\nabla \times \vec{B}_{\rm tot} = 0$). Starting from a relaxed MHD solution at $t = t_0$, the charges are sheared at constant depth along the axis of the polarity inversion line at a linearly increasing speed to reach $v_0 = 75$ km s^{-1} at time $t = 5$ minutes. The shearing motion then continues at this speed until $t = 30$ minutes when the motion is ended. Magnetic flux density at the boundary is preserved by modifying the charge strength to account for the change in distance $q_{\pm}(t) = q_{\pm,t=t_0} L_0^2/|\vec{x}_+(t) - \vec{x}_-(t)|^2$, and constant depth is maintained by utilizing motion along spherical arcs at constant radii. The shear speed in the direction of the charge motion is also applied to the velocity boundary condition in the vicinity of each charge. While clearly a very idealized model, the application of this scenario leads to the requisite onset of instability and large-scale transient, as was the case for the conditions studied by Roussev et al. (2007).

4. MODEL RUNS

In this section we present four simulation runs of the LC model for the 2008 March 25 EUV wave transient. The aim of conducting multiple simulations is to gain insight into the governing processes of EUV waves by changing important parameters, namely the average magnetosonic speed, eruption handedness, and total free energy. The varied parameters are shown in Table 1; all other considerations remain constant between the runs. For each run, a quasi steady-state coronal solution is first achieved by integrating the model in local time stepping mode (described in Cohen et al. 2008), which amounts to explicitly integrating each solution block, 64 cell volumes in this case, at its minimum timescale (a local quantity) from the initial condition for 8×10^4 iterations. At this point the eruption mechanism is applied, setting $t_0 = 18{:}40{:}00$ UT, and each run is advanced explicitly at the minimum global timescale until $t = 20{:}40{:}00$ UT physical time is reached.

Run A: baseline run. With the first run, we establish a baseline simulation for the event. In Figure 6, we show a running ratio time-series of the first 40 minutes of the synthesized images for Run A from the *STEREO-A* viewpoint. As in the observations, a bright expanding front is seen clearly off of the limb in from the *STEREO-A* perspective, as well as a similar anti-correlation of the sign of the flux ratio between the lowest temperature response filter (171 Å) and higher temperature response filters (195 Å, 284 Å, Ti-Poly), suggesting similar compression and thermodynamic mechanisms. Before proceeding we summarize the main discrepancies between the model and observations. (1) The positive enhancement is most pronounced in the higher temperature bands (284 Å and Ti-Poly) and shows less enhancement in the 195 Å band compared to typical EUV wave observations, suggesting that the initial quiet-Sun temperature at $r = 1.1\ R_{\odot}$

is likely slightly too high. (2) The width of the front observed off the limb by *STEREO-A* is less coherent (about a factor of two) in the simulation. This is likely due both to finite resolution effects as well as the inability to produce arbitrarily fast reconnection and energy release with our eruption mechanism. (3) The imposed eruption mechanism, while producing a strong transient, does not produce a fully formed erupting flux rope and strong core EUV dimming signal above the eruption site; as a result, the ejected mass is significantly less than that calculated by Aschwanden (2009). This directs our focus to the feature best represented in the simulations: the expanding front of the EUV transient, which is the wave-like component identified by Patsourakos et al. (2010). Despite these shortcomings, we propose that the ability of such a relatively simple model to capture the basic EUV properties of the expanding front represents a significant development.

Dissecting the transient signal. All simulations presented here show similar qualitative features to those described for Run A, namely a bright expanding rim showing clear temperature and density enhancements, but they differ in fundamental ways when studied in detail. As a concise and robust method of comparison, we turn to examining the transverse properties of the transient with time–distance limb diagrams (Section 2.2). In Figure 7, we show time–distance limb diagrams for an $r = 1.10\ R_{\odot}$ arc based on synthetic images for the three EUVI filters (171 Å, 195 Å, 284 Å), the XRT T-Poly filter, and EM all extracted at the *STEREO-A* location. Looking at the EM diagrams (rightmost column) all runs show a well-defined density front propagating away from the eruption site in both directions, followed by both a flattening and low amplitude reversal of the signal as the front encounters the coronal hole regions (the gradient in magnetosonic sound speed is large at this interface). The anti-correlation between the 171 Å filter and the others is best seen comparing the 171 Å diagrams to the Ti-Poly diagrams, again suggestive of an increased temperature within the transient. However, in the case of the simulations, the 195 Å also shows this anti-correlation (to a lesser extent). Here, we note that this anti-correlation signal is somewhat sensitive to both the initial plasma temperature and perturbation amplitude, as the slope of $R_i(n_e, T_e)$ for the 195 Å filter reverses around $T_e \sim 1.4$ MK. This implies that either the initial temperature of the coronal plasma at this radii is too high as compared to observations (most likely), or that the temperature perturbation has a higher amplitude than in the actual observations. Comparing the Ti-Poly diagrams to the EM diagrams also gives a means of separating the correlation of temperature to density enhancement, which are typically co-spatial, but not entirely (e.g., the leading edge of the signal of Run D).

To quantify a relative comparison of the model runs to one another, we focus in detail on the structure of the northward propagating transient as identified in the time–distance limb diagrams. Choosing a position s along the $r = 1.10\ R_{\odot}$ arc used by the time–distance diagrams gives the flux ratio as a function of time $f_s(t)$, which we show for each filter for two locations along the time–distance arc ($s_1 = 0.18$ and $s_2 = 0.70\ R_{\odot}$) for each run in Figure 8. Each trace of $f_s(t)$ exhibits an initial rise (fall in 171 Å) as the transient first arrives followed by a clear temperature and EM maximum. However, the shape of each front is modulated as it evolves in space as well as from run to run. We separate the transient signal in terms of two components: (1) a leading or "rise front" that identifies the time for a fixed location along the arc that the transient first appears, and (2) a compression peak that identifies the time of the maximum density perturbation for fixed location. Calculating the rise and
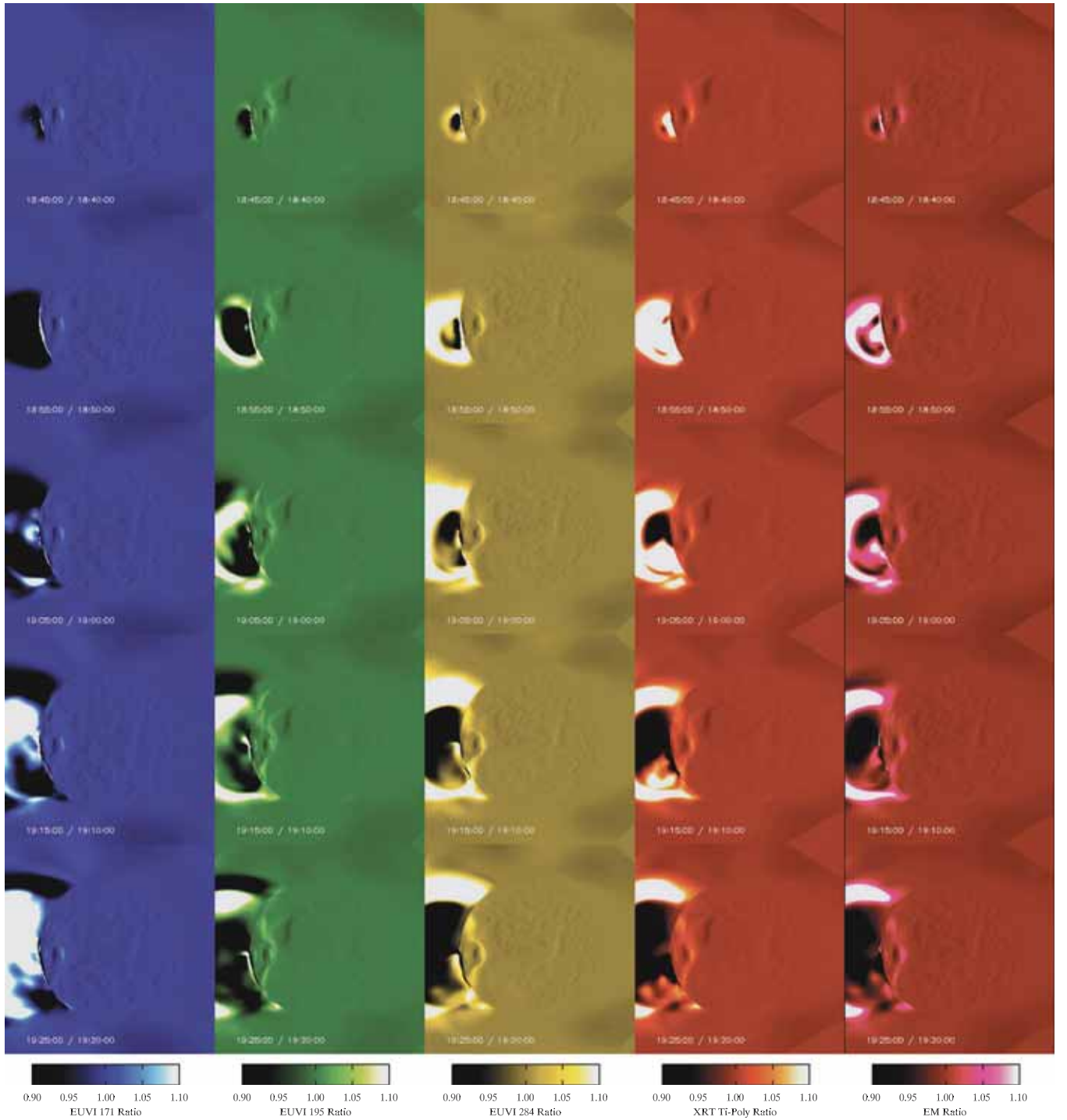
Figure 6. Five minute running ratio images showing the evolution of the EUV wave transient for Run A shown at 10 minute intervals. The columns from left to right are EUVI 171 Å, 195 Å, 284 Å filters, XRT Ti-Poly filter, and integrated EM.

compression times for multiple locations on the arc gives a means of measuring the relative speed of each component and contrasting their change from run to run.

The timing of the rise front is determined by setting a normalized threshold value, a, and determining the time t_{rise} for which $a = abs(f_s(t))/\max(abs(f_s(t)))$. The timing of the compression peak is simply the time t_{peak} for which $f_s(t) = \max(f_s(t))$ for the EM (density only) filter. The velocity of the front between two points, s_1 and s_2, is then readily determined as $v_{front} = (s_2 - s_1)/(t_2 - t_1)$, where t_1 and t_2 are determined from

the methods listed above. Estimates of the inherent variation are determined by repeating the process for the nine pairs of points between $[s_1 - \Delta s, s_1, s_1 + \Delta s]$ and $[s_2 - \Delta s, s_2, s_2 + \Delta s]$ and calculating the average v_{front} (here $\Delta s = 0.06\,R_\odot$). Because the threshold method is somewhat ill-posed, we determine the average v_{rise} by repeating averaging the above process for values of $a : [0.1, 0.15, 0.20, 0.25]$ and determine our estimate of the error in the mean v_{rise} as the difference between the minimum and maximum velocities determined here. The compression location is well defined, and we calculate the error estimate as
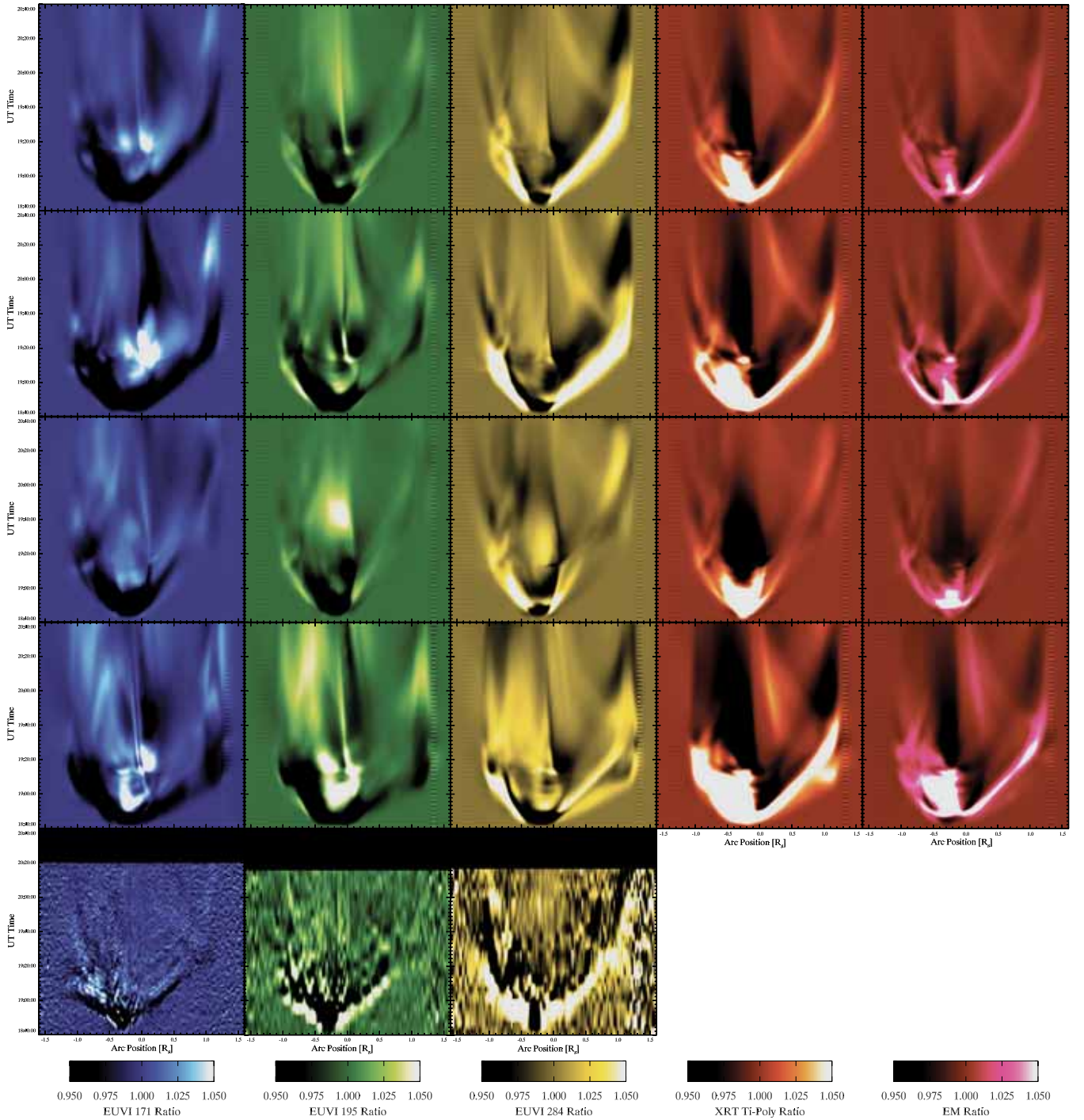
Figure 7. Time–distance diagrams at $r = 1.1\ R_{\odot}$ of the east limb for all four model runs and observations. From top to bottom we show Run A (baseline run), Run B (two times free energy), Run C (opposite handedness), Run D (two times ambient field), and EUVI-A observations. Shown in columns from left to right are the EUVI 171 Å, 195 Å, 284 Å filters, XRT Ti-Poly filter, and integrated EM. The XRT diagram provides a diagnostic of the high temperature shifts during the event, while the EM gives purely the line-of-sight density dependence. To maximize fidelity, all synthesized time–distance diagrams are at a 2.5 minute cadence (the observation diagram cadences are described in the caption of Figure 2).

the standard deviation of the nine computed values for v_{peak}. The speed determinations for each front using locations $s_1 = 0.18$ and $s_2 = 0.70\ R_{\odot}$ is summarized in Table 1.

Another feature of this diagnostic is its ready characterization of the thermodynamic response of the plasma to the transient. Looking at in detail $f_{s_1}(t)$ for Run A (top trace of Figure 8(a)), we see that the transient signal is characterized by a marked decrease in 171 Å flux, a rise then fall in 195 Å flux, and ensuing peaks in the 284 Å and Ti-Poly filters, which are co-

temporal with the peak density compression. The process is then reversed as the front passes. This is entirely consistent with the traveling front smoothly enhancing the local temperature, T_e, and shifting the spectral response functions along the curve shown in Figure 4, a mechanism proposed by Wills-Davey & Thompson (1999). It is also worth noting that the static quiet-Sun heating component (Section 3.2) is not likely to contribute significantly to these thermodynamic phenomena because its inherent heating timescale, $t_{\mathrm{heat}} \sim P_e/Q_{\mathrm{qs}}$, is greater than
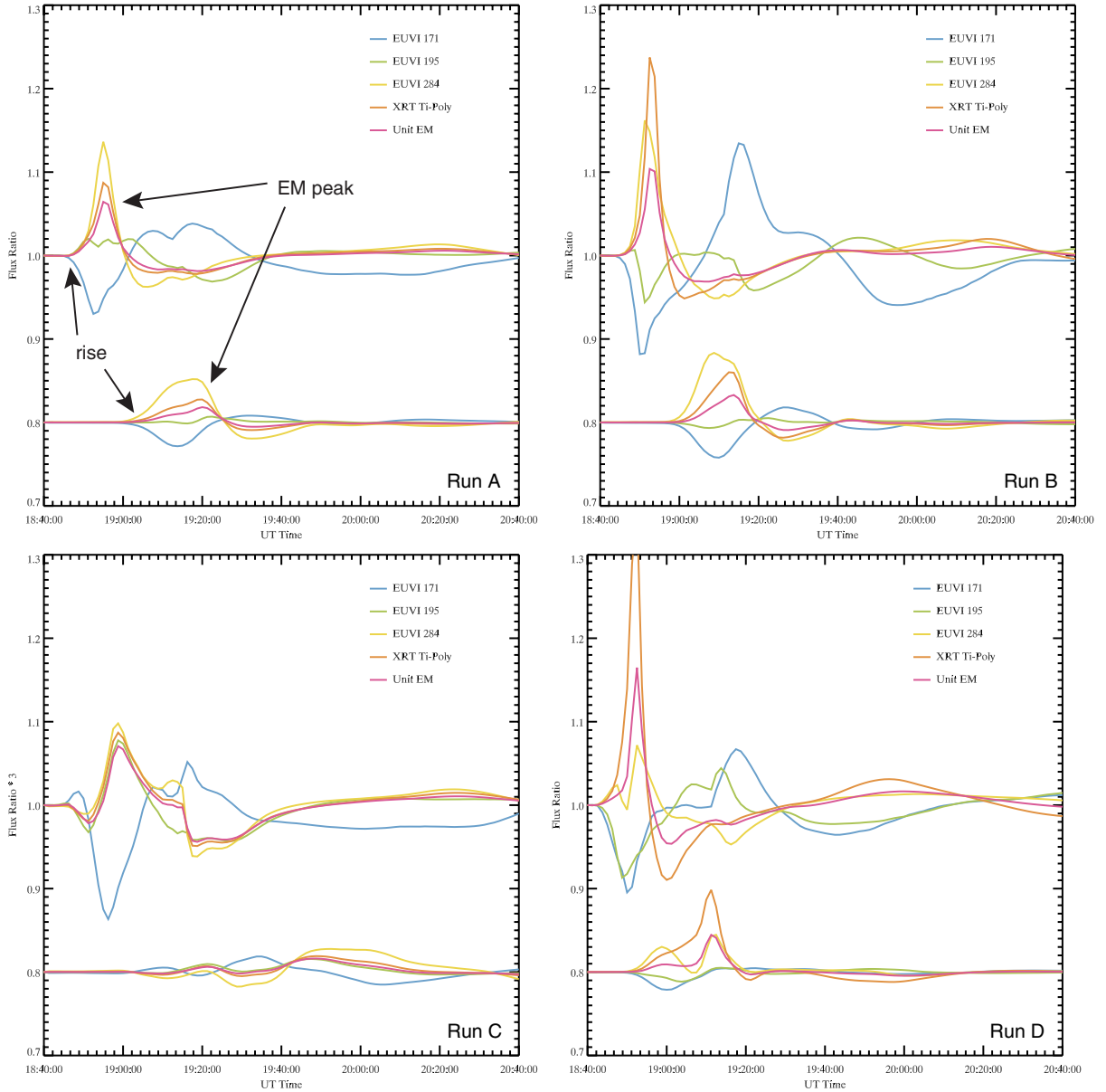
Figure 8. The flux ratio as a function of time for two points $s_1 = 0.18\,R_\odot$ (upper trace) and $s_2 = 0.70\,R_\odot$ (lower trace) on the arc axis of the time–distance diagrams (Figures 2 and 7) for Run A (baseline run), Run B (two times free energy), Run C (opposite handedness), and Run D (two times ambient field). The traces are separated by subtracting a constant offset from the flux ratio at s_2: $f_{s_2}(t) \rightarrow f_{s_2}(t) - 0.2$. The signal for Run C is scaled by a factor of three to emphasize the low-amplitude early rise front. The annotation for Run A illustrates what is identified in the front calculations for each run. The strong distortion of the perturbation signal in the lower trace for Run D is indicative of the bifurcation of the two fronts when the fast-magnetosonic speed is doubled.

30 minutes at $r = 1.1\,R_\odot$ for $n_e > 5 \times 10^{-7}\,\mathrm{erg\,cm^{-3}}$ and $T_e > 10^6$ K.

Run B: eruption strength. With our next run we choose to examine the effect that eruption strength plays in characterizing the EUV wave. To do so, we double the amount of magnetic flux involved in the shearing motion by doubling the strength of base charge to $|q_\pm| = 4 \times 10^{21}$ Gauss cm^2. To preserve nearly identical heating with respect to Run A, we subtract the additional contribution to $\vec{B}$ from the AR heating term (Q_{ar} in Equation (2)). Examining the main differences between the transient signatures of Run A and B in the time–distance diagrams (Figure 7), it seems that the dominant effect is a larger amplitude for the transient, particularly for the 284 Å and Ti-Poly bandpasses. This is consistent with the fast-mode wave interpretation, as an increase in energy released should naturally imply an increase in wave amplitude, although this

would be similarly true for more complex modes as well. However, we also observe a slight increase in transverse speed of both the rise and peak compression fronts ($\sim$50–60 km s^{-1}). The slight increase in the speed of both components is difficult to explain with a freely propagating fast-mode wave in the sub-shock limit, as is the case here. This increase suggests that the speed has been modulated due to the enhanced amplitude of the eruption and overpressure of the expanding plasma cavity, a phenomenon consistent with the solitary wave hypothesis of Wills-Davey et al. (2007). Of course, the relative importance of each mechanism cannot be easily determined yet in this case.

Run C: eruption handedness. The second variable we examine is that of eruption handedness. As discussed in Section 3.3, the photospheric motion of AR flux concentrations typically exhibits shearing patterns around the inversion line, a natural result of the Lorentz force on the atmosphere due to magnetic
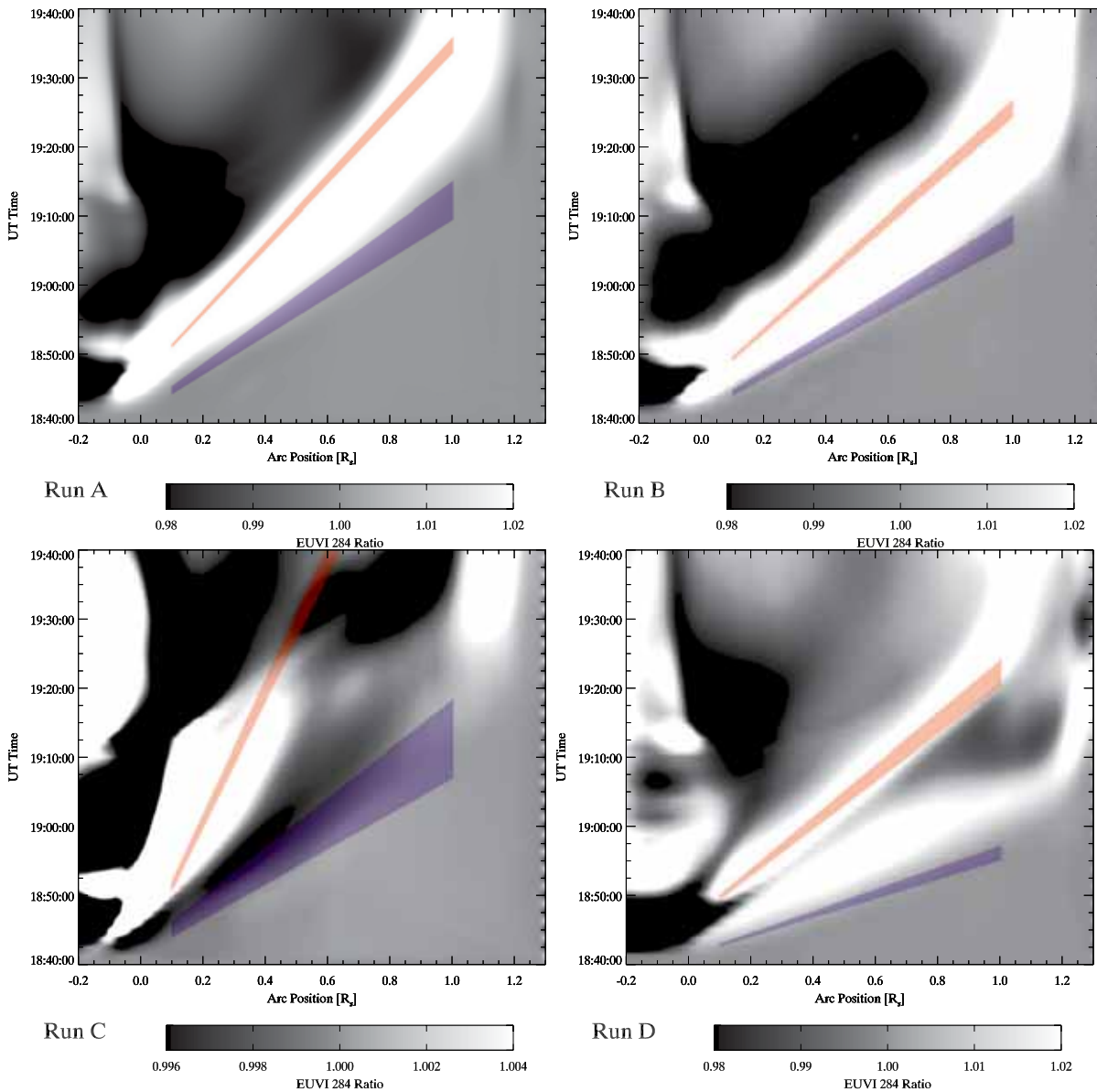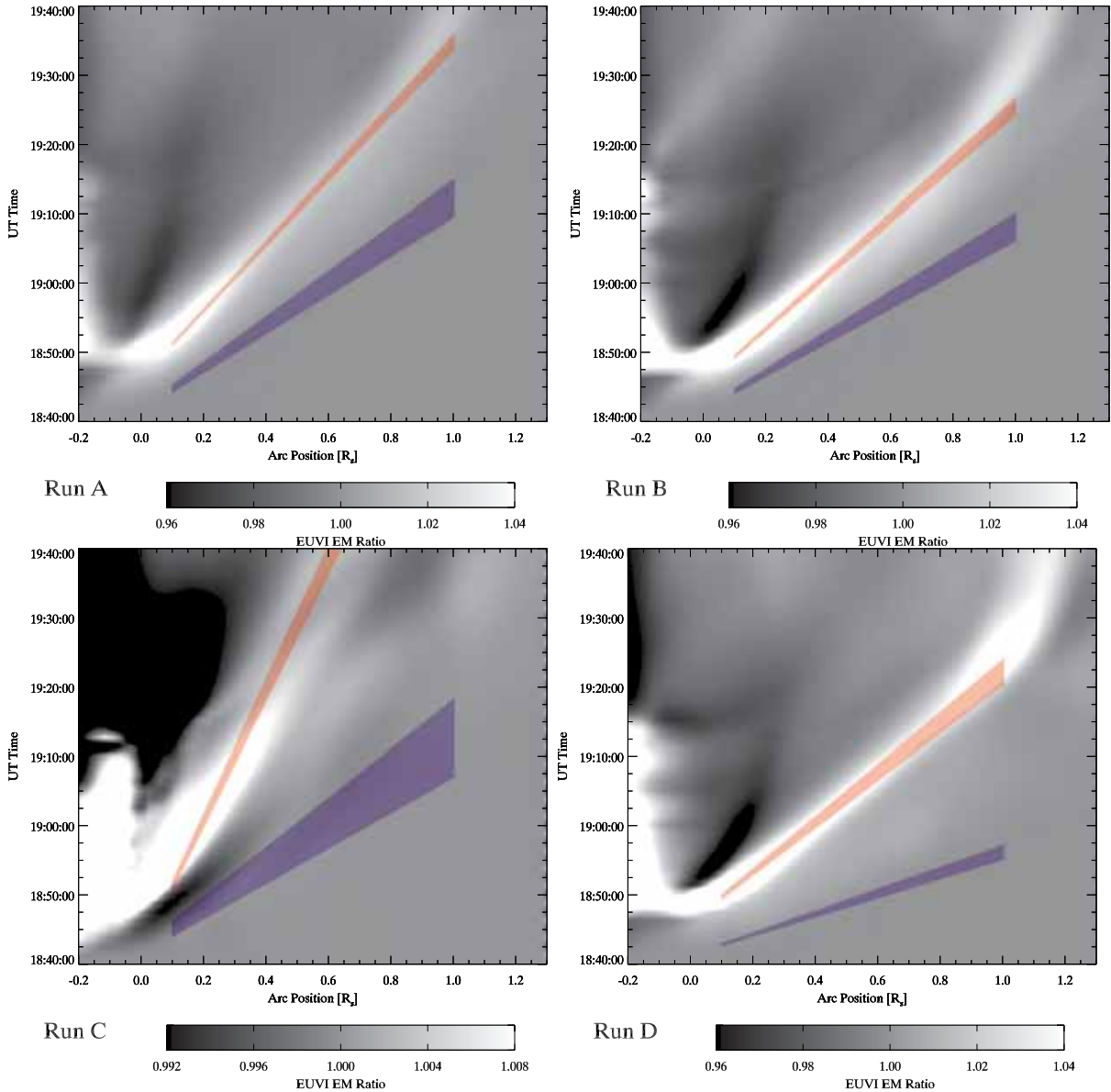
Figure 9. Time–distance diagrams of the EUV transient for all four runs zoomed in on the northward front of the EUV perturbation for the synthesized EUVI-A 284 Å filter. The transparent polygons represent the derived speed limits of the rise front (blue) and the compression peak (red) diagnostics for each run (see Table 1 for the speed ranges). Similar to Figure 3, the slope of the polygon is defined by the bounding speed range, while the width in time is defined by the time interval needed to travel at these speeds to $s = 0.1\ R_\odot$ from $s = -0.15\ R_\odot$. The left position (intersection) of the polygon on the diagram is simply the calculated $t_{\rm rise}(t_{\rm peak})$ for $s = 0.1\ R_\odot$. The contrast is enhanced to show the location at which the perturbation is first seen, which is the feature identified by the rise calculation. The separation of the two fronts for Run D is also clearly visible.

flux emergence (Manchester et al. 2004; Archontis et al. 2004). When the overlying coronal field is asymmetric, a change in sign of the shearing motion will drastically change the interaction between the two flux systems (overlying field and emerging field). In Run C, using the same relaxed configuration and heating model of Run A, we reverse the shear direction by 180° by changing the projected motion of the positive and negative charges from North/South (N/S) to South/North (S/N), respectively. As seen in Figure 7, this has a dramatic effect on both the strength and location of the resulting transient, most noticeably shifting the peak of the transverse EM signal from the northward to southward direction. Of note is the fact that the rise component of the northward transient is greatly diminished in amplitude (but not zero!), while the compression peak component remains relatively intense but travels at a markedly slower projected speed (240 km s⁻¹ in

Run A, 123 km s⁻¹ in Run C). However, the rise front travels at a nearly identical speed to that in Run A, suggesting a similar mechanism with differing amplitudes, which is consistent with the identification of this front as the fast-mode component. The difference in speed between the respective compression peaks in Run A and Run C suggests an alteration of the speed and/ or location of the global compression response of the ambient coronal field to the north, which should result naturally from a significant change in the nature of eruption brought about by reversing the shear direction.

Run D: ambient magnetosonic speed. In our final simulation, we focus on the dependence of the EUV transient properties on the ambient magnetosonic speed in the corona. For this simulation, Run D, we scale $|q_\pm|$ and the boundary magnetic field by a factor of two (thus scaling the three-dimensional PFSSM initial condition by the same factor), while simultaneously decreasing

Figure 10. Time–distance diagrams of the EUV transient for all four runs zoomed in on the northward front of the EUV perturbation for the integrated column emission measure along the limb arc. The transparent polygons are identical to those in Figure 9 and represent the derived speed limits of the rise front (blue) and the compression peak (red) diagnostics for each run. This is intended to visually highlight the fact that the peak of the enhancement is seen to propagate at a significantly lower speed (slope) than the first instance of the perturbation as derived from the EUV filters, which is at a significantly lowered amplitude when examining the column emission measure (density only).

the $\vec{B}$ dependence of the Q_{ar} heating component by the same amount. After advancing the model to steady state, we achieve a similar equilibrium to that of Run A except now the magnetic field strength everywhere has increased by roughly a factor of two. Depending on the local ratio of sound speed, c_s, to the Alfvén speed, v_A, (note $c_s^2/v_A^2 = \gamma\beta/2$, where β is the ratio of thermal pressure to magnetic pressure), this gives an increase in the perpendicular fast magnetosonic speed, $c_f = \sqrt{v_A^2 + c_s^2}$, of roughly a factor of two for low β regions (note that $\beta < 0.01$ for most of the corona below $r = 1.5\,R_\odot$, away from polarity inversion regions and current sheets), and a factor $\sim$1.66 for $\beta = 1$.

The most obvious difference between Run D and Run B (which releases a comparable amount of magnetic energy due to the identical increase in charge strength) is the increase in speed of the rise component of the transient signal by nearly a factor of two (440 km s^{-1} in Run B, 780 km s^{-1} in Run D).

Clearly, this leading edge is highly dependent on the ambient magnetosonic speed, which allows for the direct identification of the "rise-front" as the fast magnetosonic wave component of the EUV wave transient. Another striking result is the fact that the peak of the compression front shows only a slight speed increase ($\sim$10%) relative to its Run B counterpart, and Run D now shows a clear bifurcation between the two fronts (visible in Figures 7 and 8). The lack of dependence on the fast magnetosonic speed of the trailing front suggests an alternate mechanism that is tied to the inherent details and timescales of the eruption impinging on the surrounding medium itself and *not* the ambient magnetosonic speed of the medium.

5. DISCUSSION

The runs described in Section 4 provide an intriguing result. The peak transverse front of the EUV wave depends more on the inherent timescales of the CME itself, rather than the ambient
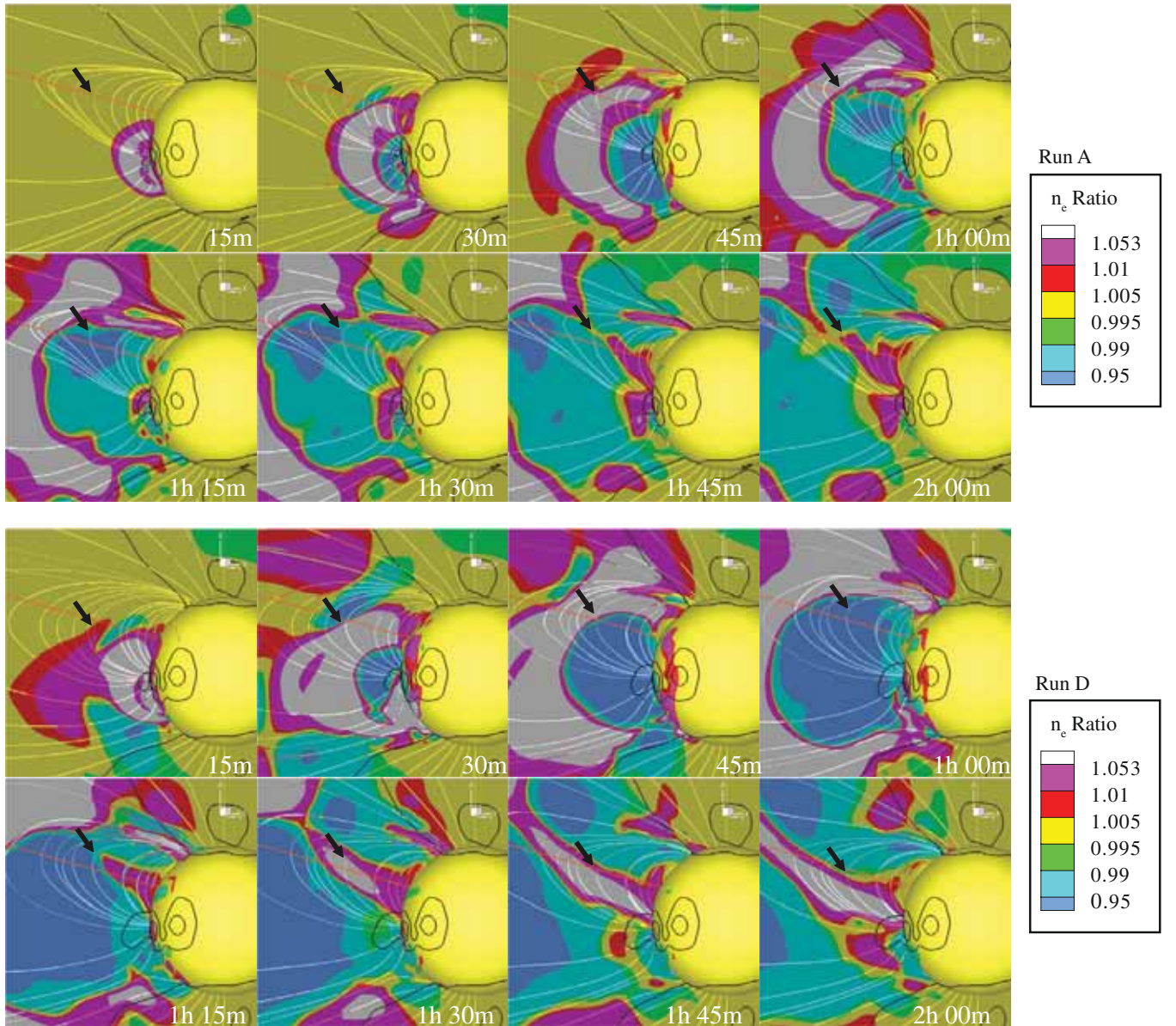
Figure 11. Visualization of the evolution and interaction of the transient with the ambient corona for the baseline run (Run A, top) and the run with magnetic field scaled by a factor of two (Run D, bottom) at 15 minute intervals for the first 2 hr of the event. Coloring indicates 5 minute running ratios of the electron density, n_e, on an $r = 1.10\ R_\odot$ surface and the plane normal to the *STEREO-A* viewing vector. Three-dimensional streamtraces of $\vec{B}$ are drawn from points intersecting this plane and the spherical surface at near equal latitude intervals and the same points are used in each frame. These are chosen to emphasize the interaction of the expanding CME front and compression of the northward streamer region. This is highlighted by comparing the streamlines from frame to frame to the fixed orange line drawn as a reference point. The black arrow in each frame is hand drawn to point to the apex of a selected streamtrace ($|B_r| \sim 0$) and also illustrates the shift in this position as a function of time. The black lines show the contours of $c_f = (1000, 3000)$ km s^{-1} for Run A and $c_f = (2000, 6000)$ km s^{-1} for Run D, which serve to outline the ARs and latitudinal extent of the polar coronal holes.

sound speed of the entire corona—a *key* distinction. This falls directly in line with an identification of the peak compression front as the nonlinear response of the ambient coronal structure to the expansion of the eruption itself, which is in line with the "driven MHD-wave/plasma compression" scenario, one of two plausible scenarios emphasized by Attrill et al. (2009). This is further supported by the discrepancy of the compression peak speed (v_{peak}) with the rise speed (v_{rise}) for every run, where v_{rise} is consistently larger by at least 100 km s^{-1}. To show this visually, we plot time–distance diagrams for each run zoomed in on the northward propagating perturbation with overplotted derived front speed ranges for the EUVI-A 284 Å filter (Figure 9) and column EM (Figure 10).

Focusing now on the three-dimensional simulation data directly, we show the evolution of the front and ambient magnetic topology on an $r = 1.10\ R_\odot$ surface and plane normal to the *STEREO-A* viewing position for Runs A and D in Figure 11. The running ratio contours of n_e show that a hemispherical perturbation ($\pm \sim 5\%$–10%) propagates away from the erupting AR, forming a coherent outwardly propagating front. The separation of the fast-mode front from the coherent front formed by the eruption becomes quite evident comparing the initial 30 minutes (first two frames) of Runs A–D. The increase in magnetic free energy released (due to the doubling of $|\vec{B}|$ everywhere) has also modulated the outward speed of the compression front approximately 20%–50% but is this not the near
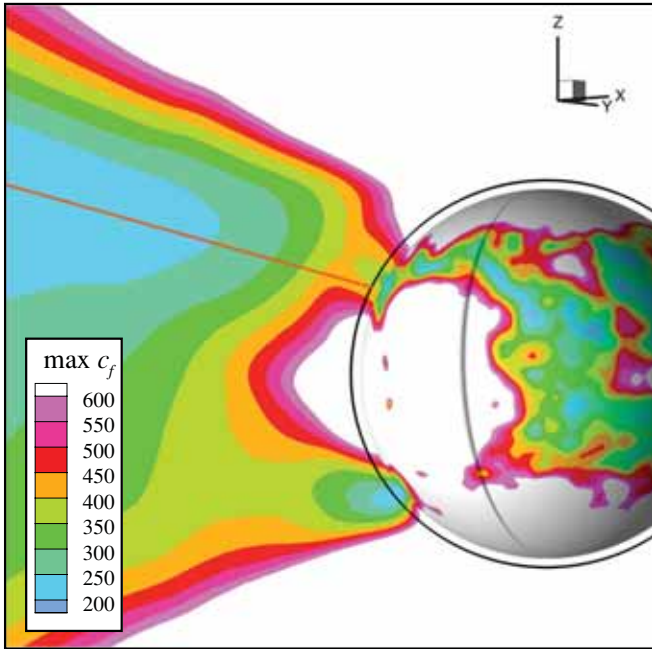
Figure 12. Color contours of the maximum (perpendicular) fast magnetosonic speed, $c_f^{\max} = \sqrt{V_a^2 + c_s^2}$, in units of km s^{-1} for the pre-eruption configuration of Run A showing the same plane as in Figure 11 and an iso-surface of $r = 1.05\,R_\odot$ (note $c_f^{\max} \sim v_a$ for $\beta \ll 1$). The black line indicates $r = 1.1\,R_\odot$ (the same distance of the time–distance diagrams) and the fixed orange line from Figure 11 is shown. Note that $c_f^{\max} > 350$ km s^{-1} along the entire $r = 1.1\,R_\odot$ arc northward of the eruption region, while the derived speed of the transverse compression peak for Run A is $\sim$240 km s^{-1}. The saturation value of 600 km s^{-1} is chosen to illustrate the topological regions where c_f is large.

factor of two as would be expected by the increase in magnetosonic speed. This provides further evidence that the bulk of the perturbation signal is a result of the compression induced by the eruption processes and propagating plasma cavity, which will have a nonlinear relationship to the overall characteristic sound speeds of the corona.

Additional evidence for an organized transverse compression front comes from examining the effect of the eruption on the northward streamer region, visualized with magnetic streamlines in Figure 11. The orange line, which remains constant in each frame, represents the axis of the streamer region intersecting this plane for the pre-eruption state of Run A (i.e., $B_r \equiv \vec{B} \cdot \hat{x} \sim 0$). As the peak amplitude of the front passes around $t \sim 45$–75 minutes, the axis of the streamer region shifts northward collectively, and becomes noticeably offset from its equilibrium position (highlighted by the arrows). As the eruption front moves outward, and subsequently exits this region of the corona ($t > 75$ minutes), the axis of the streamer region is seen returning to its original position, co-temporal with the density front now traveling in the opposite, southward direction (most noticeable in Run D due to the increased eruption speed and amplitude). This implies that the observed EUV wave signal is most closely related to the plasma compression of the streamer region (surrounding field) as it is perturbed from an equilibrium state.

It is also worth noting that in these simulations we are probing a regime where the transverse speed of the compression front in the quiet-Sun is below the typical fast magnetosonic speed. This is illustrated by showing the maximum (perpendicular) value of the fast magnetosonic speed, $c_f^{\max} = \sqrt{V_a^2 + c_s^2}$, on the same plane shown in Figure 11 for the pre-eruption state of

Run A in Figure 12. The fact that $c_f^{\max} > 350$ km s^{-1} along the entire $r = 1.1\,R_\odot$ arc northward of the eruption region indicates that the transverse compression peak ($\sim$240 km s^{-1}) is indeed traveling well below the fast magnetosonic speed (note that $c_f^{\max}$ effectively doubles everywhere for Run D so this statement is still valid). If the conditions were reversed and the ambient Alfvén speed was significantly lower than the transverse evolution of the event, the formation and propagation of shocks would indeed modify the results (i.e., the case in the rising flux-rope experiment of Wang et al. 2009 or the scenario outlined in Veronig et al. 2010), which we leave to a further investigation. In our case, using a smoothed MDI magnetogram for the PFSSM initial condition and magnetic boundary conditions in the model is likely to *underestimate* the average magnetic field strength and thus fast magnetosonic speed in the quiet corona. This, combined with the realistic thermodynamic conditions afforded by the LC model (supported by the observation comparison shown in Figure 5), suggests that these sub-shock conditions are a plausible limit for the true quiet corona.

6. CONCLUSIONS

Using a global MHD model of the low corona as an experimental laboratory, we have studied the effect of three critical parameters on the subsequent evolution of the EUV transient, namely the eruption strength, eruption handedness, and ambient sound speed of the corona. Additionally, by modeling the realistic conditions of an observed event (instead of an idealized or axisymmetric case), we have a means of interpreting the features and discrepancies of the results in direct context with observed characteristics of EUV waves, while simultaneously including the same form of observational bias. While it is obvious that these three variables should all play a role in determining the EUV wave characteristics, the separation of all three in a cohesive manner allows for the following interpretations.

1. We can decompose the EUV wave transient into two parts: (1) a rise component traveling at the fast-mode speed, and (2) a separate (but often nearly overlapping) compression front of the surrounding medium brought about by the expansion of the erupting structures into the corona, which constitutes the diffuse peak of an EUV wave transient. This interpretation, one which identifies the EUV signal as a driven nonlinear compressional wave, relaxes the requirement that this diffuse peak travels at the fast magnetosonic speed. This a very similar distinction to those made by Chen et al. (2005) and Cohen et al. (2009), and in this case we do not require a freely propagating fast-mode component traveling at the fast magnetosonic speed to explain the coherent characteristics of the observed transient front (though it must surely exist at some amplitude).

2. The amount of energy released during the eruption has a strong enhancement effect on the amplitude of the transient, but a lesser effect on the overall speed (which should be related to the nonlinear scaling of the eruption speed with free energy).

3. Altering the eruption handedness strongly dictates the shape and speed of the peak compression front. However, the fast-mode front retains a similar speed and location (though with considerably less amplitude) again suggesting that the two components are independent.

4. Through direct synthesis of observations we are able to recreate and examine the contrasting multi-filter

14

dependence of the EUV wave transient. We find that the anti-correlation of the perturbation amplitude between 171 Å (lessened emission) and the 195 Å and 284 Å filters (enhanced emission) can be well represented by temperature enhancement inside a propagating compression front, which is also diffusive due to the electron heat conduction term. We do not find that reconnection and/or permanent mass depletion are necessary components for describing these phenomena, though it should certainly modulate the signal where and when it does occur.

5. Increasing the ambient sound speed in the corona caused a clear separation of the two identified components, with the dominant transient component traveling below the fast-mode speed. This is a direct test of the fast-magnetosonic wave hypothesis and, in these experiments, we find that the freely propagating fast-mode wave is not significantly contributing to the large-scale transverse signal of an "EUV wave." This places emphasis on the need for any unified interpretation of the EUV wave picture to also account for the dynamic response of the global corona to the triggering eruption.

Of course, with the commissioning phase of the Atmospheric Imaging Assembly (AIA; Rochus et al. 2004) on board the *Solar Dynamics Observatory* nearing completion, we are poised to explore EUV waves with revolutionary observational advances in both time and temperature cadence. As such it is important to strive to develop models that are able to both capture observations and interpret the underlying mechanisms that compose them.

REFERENCES

Altschuler, M. D., Levine, R. H., Stix, M., & Harvey, J. 1977, Sol. Phys., 51, 345

Archontis, V., Moreno-Insertis, F., Galsgaard, K., Hood, A., & O'Shea, E. 2004, A&A, 426, 1047

Aschwanden, M. J. 2009, Ann. Geophys., 27, 3275

Aschwanden, M. J., Nitta, N. V., Wuelser, J., Lemen, J. R., Sandman, A., Vourlidas, A., & Colaninno, R. C. 2009, ApJ, 706, 376

Attrill, G. D. R. 2010, ApJ, 718, 494

Attrill, G. D. R., Engell, A. J., Wills-Davey, M. J., Grigis, P., & Testa, P. 2009, ApJ, 704, 1296

Attrill, G. D. R., Harra, L. K., van Driel-Gesztelyi, L., & Démoulin, P. 2007, ApJ, 656, L101

Chen, P. F., Fang, C., & Shibata, K. 2005, ApJ, 622, 1202

Chen, P. F., Wu, S. T., Shibata, K., & Fang, C. 2002, ApJ, 572, L99

Cohen, O., Attrill, G. D. R., Manchester, W. B., & Wills-Davey, M. J. 2009, ApJ, 705, 587

Cohen, O., Sokolov, I. V., Roussev, I. I., & Gombosi, T. I. 2008, J. Geophys. Res., 113, A03104

Cohen, O., et al. 2007, ApJ, 654, L163

Dai, Y., Auchere, F., Vial, J. C., Tang, Y. H., & Zong, W. G. 2010, ApJ, 708, 913

Delaboudinière, J.-P., et al. 1995, Sol. Phys., 162, 291

Downs, C., Roussev, I. I., van der Holst, Lugaz N., Sokolov, I. V., & Gombosi, T. I. 2010, ApJ, 712, 1219

Freeland, S. L., & Handy, B. N. 1998, Sol. Phys., 182, 497

Gopalswamy, N., et al. 2009, ApJ, 691, L123

Howard, R. A., et al. 2008, Space Sci. Rev., 136, 67

Jacobs, C., Roussev, I. I., Lugaz, N., & Poedts, S. 2009, ApJ, 695, L171

Kaiser, M. L., Kucera, T. A., Davila, J. M., St, Guhathakurta, M., & Christian, E. 2008, Space Sci. Rev., 136, 5

Khan, J. I., & Aurass, H. 2002, A&A, 383, 1018

Klassen, A., Aurass, H., Mann, G., & Thompson, B. J. 2000, A&AS, 141, 357

Landi, E., Zanna, D. G., Young, P. R., Dere, K. P., Mason, H. E., & Landini, M. 2006, ApJS, 162, 261

Lionello, R., Linker, J. A., & Mikic, Z. 2001, ApJ, 546, 542

Lionello, R., Linker, J. A., & Mikic, Z. 2009, ApJ, 690, 902

Long, D. M., Gallagher, P. T., McAteer, R. T. J., & Bloomfield, D. S. 2008, ApJ, 680, L81

Lugaz, N., Vourlidas, A., Roussev, I., & Morgan, H. 2009, Sol. Phys., 256, 269

Ma, S., et al. 2009, ApJ, 707, 503

Manchester, W., IV, Gombosi, T., Dezeeuw, D., & Fan, Y. 2004, ApJ, 610, 588

Mok, Y., Mikic, Z., Lionello, R., & Linker, J. A. 2005, ApJ, 621, 1098

Moses, D., et al. 1997, Sol. Phys., 175, 571

Pevtsov, A. A., Fisher, G. H., Acton, L. W., Longcope, D. W., Johns-Krull, C. M., Kankelborg, C. C., & Metcalf, T. R. 2003, ApJ, 598, 1387

Patsourakos, S., & Vourlidas, A. 2009a, ApJ, 700, L182

Patsourakos, S., Vourlidas, A., & Kliem, B. 2010, A&A, 522, A100

Patsourakos, S., Vourlidas, A., Wang, Y. M., Stenborg, G., & Thernisien, A. 2009b, Sol. Phys., 259, 49

Rochus, P. L., et al. 2004, Proc. SPIE, 5171, 53

Roussev, I. I., Lugaz, N., & Sokolov, I. V. 2007, ApJ, 668, L87

Roussev, I. I., et al. 2003, ApJ, 595, L57

Sheeley, N. R., et al. 2008, ApJ, 674, L109

Schmidt, J. M., & Ofman, L. 2010, ApJ, 713, 1008

Schrijver, C. J., Sandman, A. W., Aschwanden, M. J., & Derosa, M. L. 2004, ApJ, 615, 512

Thompson, B. J., et al. 1999, ApJ, 517, L151

Tóth, G., et al. 2005, J. Geophys. Res., 110, A12226

Veronig, A. M., Muhr, N., Kienreich, I. W., Temmer, M., & Snak, B. V. 2010, ApJ, 716, L57

Wang, H., Shen, C., & Lin, J. 2009, ApJ, 700, 1716

Warmuth, A., Mann, G., & Aurass, H. 2005, ApJ, 626, L121

Wills-Davey, M. J., & Attrill, G. D. R. 2009, Space Sci. Rev., 149, 325

Wills-Davey, M. J., Deforest, C. E., & Stenflo, J. O. 2007, ApJ, 664, 556

Wills-Davey, M. J., & Thompson, B. J. 1999, Sol. Phys., 190, 467

Wu, S. T., Zheng, H., Wang, S., Thompson, B. J., Plunkett, S. P., Zhao, X. P., & Dryer, M. 2001, J. Geophys. Res., 106, 25089

Wuelser, J., et al. 2004, Proc. SPIE, 5171, 111

Yang, H., & Chen, P. 2010, Sol. Phys., 266, 59